

ON THE UNIVERSALITY OF STAR FORMATION EFFICIENCY IN GALAXIES

AVA POLZIN ^{1,*}, ANDREY V. KRAVTSOV ^{1,2,3}, VADIM A. SEMENOV ⁴, AND NICKOLAY Y. GNEDIN ^{1,2,5}

¹Department of Astronomy & Astrophysics, The University of Chicago, Chicago, IL 60637 USA

²Kavli Institute for Cosmological Physics, The University of Chicago, Chicago, IL 60637 USA

³Enrico Fermi Institute, The University of Chicago, Chicago, IL 60637 USA

⁴Center for Astrophysics, Harvard & Smithsonian, 60 Garden St, Cambridge, MA 02138, USA and

⁵Fermi National Accelerator Laboratory, Batavia, IL 60510, USA

Version December 6, 2024

ABSTRACT

We analyze high-resolution hydrodynamics simulations of an isolated disk dwarf galaxy with an explicit model for unresolved turbulence and turbulence-based star formation prescription. We examine the characteristic values of the star formation efficiency per free-fall time, ϵ_{ff} , and its variations with local environment properties, such as metallicity, UV flux, and surface density. We show that the star formation efficiency per free-fall time in ≈ 10 pc star-forming regions of the simulated disks has values in the range $\epsilon_{\text{ff}} \approx 0.01 - 0.1$, similar to observational estimates, with no trend with metallicity and only a weak trend with the UV flux. Likewise, ϵ_{ff} estimated using projected patches of 500 pc size does not vary with metallicity and shows only a weak trend with average UV flux and gas surface density. The characteristic values of $\epsilon_{\text{ff}} \approx 0.01 - 0.1$ arise naturally in the simulations via the combined effect of dynamical gas compression and ensuing stellar feedback that injects thermal and turbulent energy. The compression and feedback regulate the virial parameter, α_{vir} , in star-forming regions, limiting it to $\alpha_{\text{vir}} \approx 3 - 10$. Turbulence plays an important role in the universality of ϵ_{ff} because turbulent energy and its dissipation are not sensitive to metallicity and UV flux that affect thermal energy. Our results indicate that the universality of observational estimates of ϵ_{ff} can be plausibly explained by the turbulence-driven and feedback-regulated properties of star-forming regions.

Subject headings: Galaxies – Star formation — numerical simulations

1. INTRODUCTION

It has been known for about five decades that the efficiency with which gas is converted into stars in star-forming regions (the star formation efficiency) is small (e.g., Zuckerman & Evans 1974). Over the past two decades, observations showed that star formation efficiency per free-fall time is only a few percent for a wide range of environments and scales (e.g., Krumholz & Tan 2007; Krumholz et al. 2012; García-Burillo et al. 2012; Evans et al. 2014; Utomo et al. 2018; Pokhrel et al. 2021; Hu et al. 2022; Sun et al. 2023; Mattern et al. 2024, see Section 3.2 of Krumholz et al. 2019 for a review).

Theoretical models aiming to explain the low efficiency on the scales of star-forming regions (see McKee & Ostriker 2007; Krumholz 2014, for reviews) include magnetic pressure support against collapse of gas (e.g., Mouschovias 1976a,b; Price & Bate 2009; Krumholz & Federrath 2019) and supersonic turbulence (e.g., Elmegreen 2002; Krumholz & McKee 2005), possibly mediated by magnetic fields (e.g., Padoan et al. 2012; Federrath & Klessen 2013; Federrath 2015; Girma & Teyssier 2024).

On kiloparsec and larger scales galaxies also form stars inefficiently, which is partly related to the local efficiency per free-fall time (e.g., Krumholz et al. 2012; Semenov et al. 2018). The connection between efficiency in star-forming regions and star formation rate measured on large scales arises because the local inefficiency of star-forming regions and their short lifetimes result in only a small fraction of gas being converted into stars in each star-forming region. Therefore, a given gas parcel has to go through a large number of star formation-dispersal cycles, each taking $\approx 50 - 100$ Myr as ISM atoms

make their way into a star-forming region (Semenov et al. 2017).

In this paper, we examine the dependence of the star formation efficiency per free-fall time, ϵ_{ff} , on local properties (metallicity, UV radiation field, and density of gas and stars) in a suite of high-resolution simulations that recover observed star formation properties of nearby dwarf galaxies (Kruijssen et al. 2019; Semenov et al. 2021). We show that simulations naturally produce values of ϵ_{ff} in the range $\approx 0.01 - 0.1$ close to the values estimated for observed star-forming clouds in regions of very different metallicity, UV flux, and density. We show that turbulence and stellar feedback play a key role in producing universal ϵ_{ff} values as they regulate the virial parameter of star-forming regions to a fairly narrow range. This is consistent with a picture of self-regulation of star formation via rapid dispersal of star-forming gas in a turbulent ISM.

The paper is laid out as follows: in Section 2, we describe the simulation used in this analysis; in Section 3, we examine the relationship between star formation parameters and local galaxy properties; and in Appendix A, we investigate the role of turbulence in regulating star formation. We discuss and summarize our results in sections 4 and 5, respectively.

2. SIMULATIONS

We use a suite of simulations of an isolated disk galaxy adopting initial conditions similar to the properties of the NGC 300 galaxy (Semenov et al. 2021). These simulations are run using the ART N-body+hydrodynamics code (Kravtsov 1999; Kravtsov et al. 2002; Rudd et al. 2008; Gnedin & Kravtsov 2011) and include self-consistent modeling of radiative transfer (RT; Gnedin 2014), non-equilibrium chemistry of hydrogen, helium, and molecular hydrogen, as well as realistic pre-

*apolzin@uchicago.edu

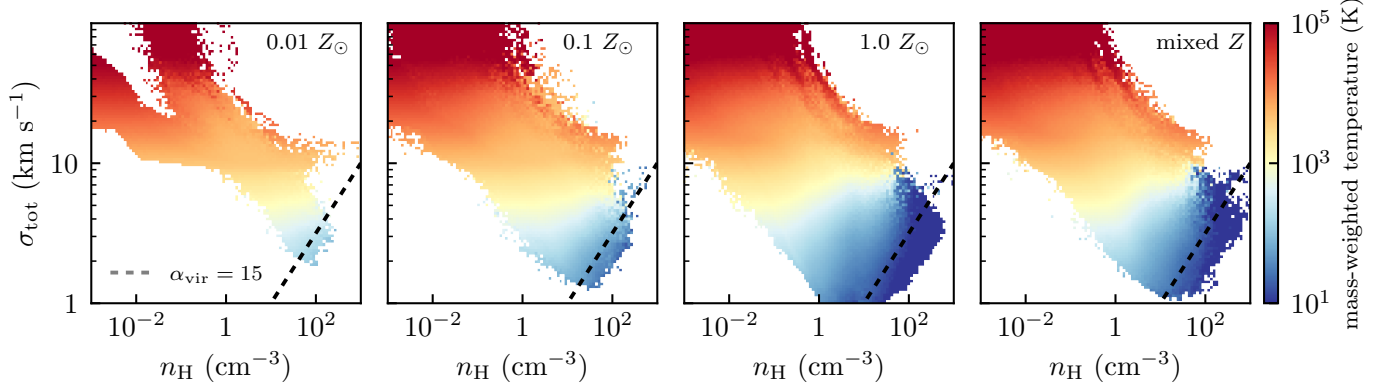


FIG. 1.— The gas mass-weighted $\sigma_{\text{tot}} - n$ phase space for four of our simulation runs. The color indicates gas temperature (see side color bar). The figure shows gas with the highest star formation rate (roughly $\alpha_{\text{vir}} \lesssim 15$) has temperatures (10–30 K) and densities (10–1000 cm^{-3}), which is similar to the typical temperatures and densities of observed star-forming giant molecular clouds when averaged on similar scales. As discussed in Polzin et al. (2024), the low metallicity runs have a lower star formation rate, not because ϵ_{ff} is intrinsically lower in low Z gas, but because the *amount* of cold, dense gas decreases.

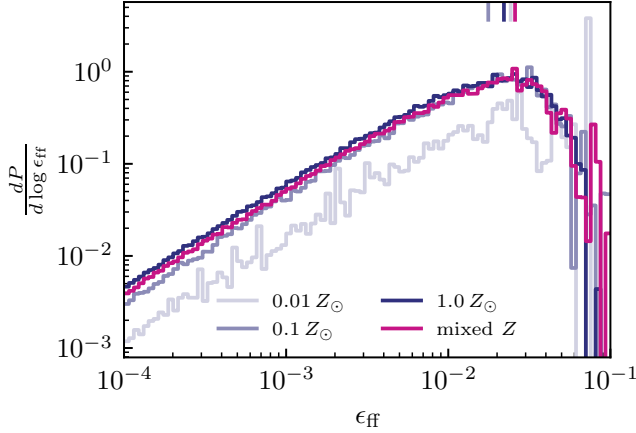


FIG. 2.— The probability density function of star formation-weighted star formation efficiency per free-fall time in four representative simulation runs. Median values are shown as vertical lines near the top of the figure and demonstrate that there is a \sim universal characteristic ϵ_{ff} of a few percent in the simulations. The low ϵ_{ff} tail in $dP/d \log \epsilon_{\text{ff}}$ persists with the same slope even below the range shown here.

descriptions for star formation and feedback. The latter is sufficiently realistic to replicate detailed properties of star forming regions in NGC 300 (Semenov et al. 2021), and the resolution ($\Delta x = 10$ pc in the highest refinement level grid cells, where most star formation is occurring) is sufficient to model feedback-regulated density fluctuations in the simulated interstellar medium.

In these simulations, the star particles form stochastically using the rate $\dot{\rho}_\star = \epsilon_{\text{ff}} \rho_g / t_{\text{ff}}$, where ρ_g is gas density, t_{ff} is the free-fall time, and ϵ_{ff} is the star formation efficiency per free-fall time. The latter is assumed to be an exponential function of the local virial parameter α_{vir} (Padoan et al. 2012):

$$\epsilon_{\text{ff}} = \exp(-\sqrt{\alpha_{\text{vir}}/0.53}) \quad (1)$$

Here the virial parameter, α_{vir} , is defined following Bertoldi & McKee (1992) such that

$$\alpha_{\text{vir}} = \frac{9.35 (\sigma_{\text{tot}}/10 \text{ km s}^{-1})^2}{(n/100 \text{ cm}^{-3}) \times (\Delta x/40 \text{ pc})^2} \quad (2)$$

where the total sub-grid velocity dispersion, $\sigma_{\text{tot}} = \sqrt{\sigma_t^2 + c_s^2}$,

includes contributions of both turbulence and the thermal energy of the gas. Note that the virial parameter depends on both the gas temperature through the sound speed and on the turbulent velocity dispersion. This, for example, prevents star formation in the warm gas ($T \gtrsim 10^3$ K). Note also that there is no explicit dependence of ϵ_{ff} on the Mach number because no significant dependence on the Mach number was found in simulations by Padoan et al. (2012) and more recent simulations by Brucy et al. (2024). Figure 1 shows the $\sigma_{\text{tot}} - n$ phase space in our simulations. The dashed line shows the constant value of $\alpha_{\text{vir}} = 15$, below which most of the star formation occurs. The figure shows that with the prescription we use in our simulations stars form in cold gas ($T \sim 10 - 30$ K) with densities of $n \sim 10 - 1000^3 \text{ cm}^{-3}$ similar to the densities of observed star-forming molecular clouds averaged on similar scales (tens of parsecs). It also shows that the star-forming gas is different than the gas selected above a constant density and or below a given temperature threshold.

The local value of ϵ_{ff} in simulation cells evolves with the evolution of the interstellar medium, based on its density and the level of turbulence on small scales. The latter is modeled using an explicit subgrid turbulence model (Semenov et al. 2016).

To isolate the dependence of the results on gas metallicity, we ran a series of simulations in which metallicity in all cells is fixed throughout the simulation. Specifically, we ran simulations in which metallicity of all cells was fixed to $0.01Z_\odot$, $0.03Z_\odot$, $0.1Z_\odot$, $0.2Z_\odot$, $0.3Z_\odot$, $0.6Z_\odot$, and $1Z_\odot$ at all times during the run (Polzin et al. 2024). This is in addition to the original run initialized with the metallicity profile matching the observed radial metallicity profile of NGC 300 and with on-the-fly enrichment turned on (Semenov et al. 2021). For comparison, we also re-ran these simulations without the sub-grid turbulence model, so that the contribution of turbulence to α_{vir} is ignored.

3. RESULTS

3.1. Star formation efficiency as a function of metallicity on ~ 10 pc scale

The main result of our analyses is that the values of star formation efficiency per free-fall time in the star-forming regions of our simulations are confined to the range $\sim 0.01 - 0.1$ with no or little dependence on the local metallicity and UV flux.

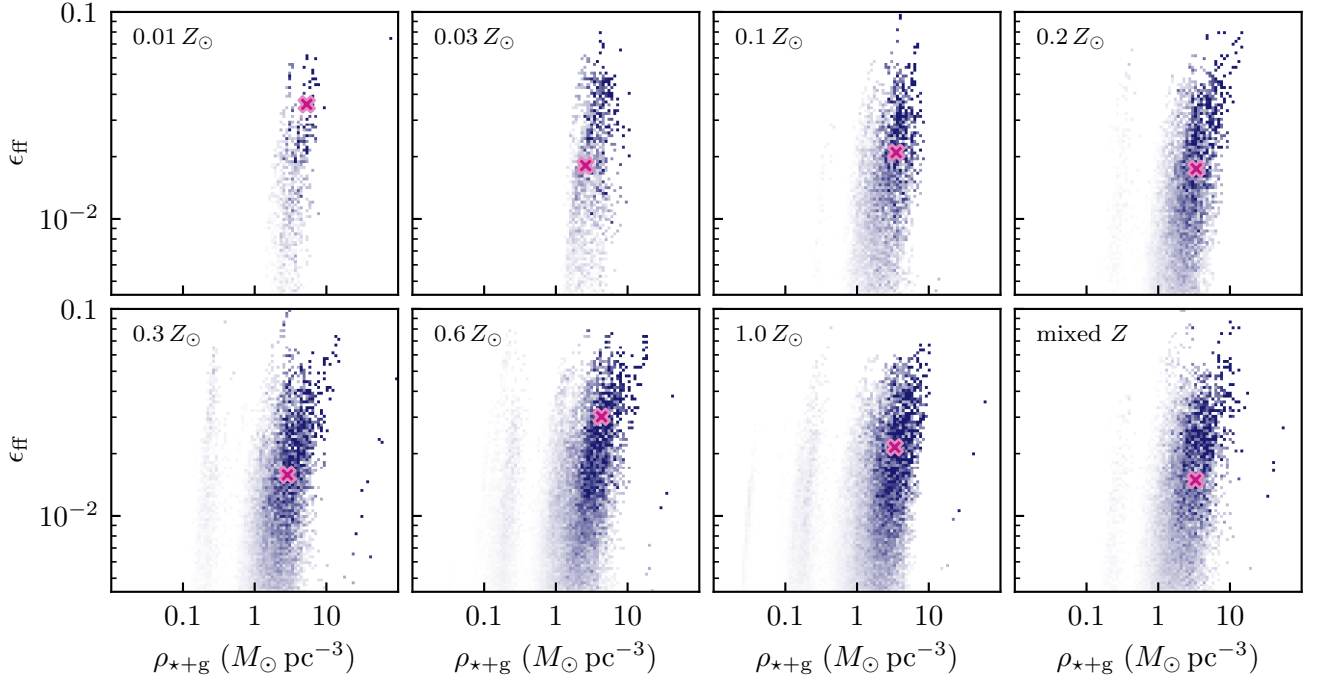


FIG. 3.— The star formation rate-weighted star formation efficiency per free-fall time, ϵ_{ff} , as a function of density of gas and stars in individual simulation cells for each of individual runs. The shading indicates the density of the simulation cells with given values of efficiency and density, linearly scaled between the 5th and 95th percentiles of the distribution for each run. Ridges at different densities are associated with different refinement levels in the simulation. Magenta crosses are placed at the star formation rate-weighted median ϵ_{ff} and $\rho_{\star+g}$ of the star-forming grid cells.

Figure 2 shows the probability density distribution of ϵ_{ff} values in the simulations of different gas phase metallicity. The distribution of ϵ_{ff} arises from the distribution of α_{vir} values in the simulations. The figure shows that the peak of the PDF and its medians occur in similar ranges at different metallicities.

Although the distribution extends to very low ϵ_{ff} values, the contribution of low- ϵ_{ff} regions to the total star formation rate is small. Moreover, results of star-forming cloud simulations of Padoan et al. (2012) used to set local ϵ_{ff} in our simulations were calibrated only at $\alpha_{\text{vir}} \lesssim 15$. Thus, in the rest of our analysis we focus on the *star-forming* grid cells contributing the bulk of star formation in regions of $\alpha_{\text{vir}} \leq 15$ or $\epsilon_{\text{ff}} \gtrsim 4 \times 10^{-3}$.

Figure 3 shows the distribution of star formation efficiency per free-fall time as a function of the baryon density (defined here as the density of stars and gas) in our simulation in grid cells (with sizes of $\approx 10 - 30$ pc). These 2D histograms are weighted by the local SFR in each cell to show the parameter space that contributes most to the total star formation rate.

The figure shows that the star-formation weighted efficiency per free-fall time has typical values of $\epsilon_{\text{ff}} \sim 0.01 - 0.1$, which is similar to the range estimated in observations (e.g., Krumholz & Tan 2007; García-Burillo et al. 2012; Evans et al. 2014; Agertz & Kravtsov 2015), and that the range of efficiencies does not depend on the density.

We note these characteristic efficiency values are not a result of tuning but arise naturally in simulations (see Section 4 for discussion). Furthermore, the top panels in Figures 4 and Figure 5 show that the characteristic ϵ_{ff} range does not depend on gas metallicity and depends only very weakly on free-space¹ UV flux, U_{MW} , normalized by the Milky Way value at

1000 Å (Draine 1978; Mathis et al. 1983).

Remarkably, while the amount of star-forming gas decreases with decreasing metallicity due to increasingly inefficient cooling (see Polzin et al. 2024, for a detailed discussion), the range of ϵ_{ff} remains the same for all simulated metallicities. In what follows we show that ϵ_{ff} also has no, or very weak, dependence on the averaging scale and other properties of the local galactic environment.

Figures 4 and Figure 5 also show the averages and characteristic range of the local depletion time of the gas in simulations cells, $t_{\text{ff}}/\epsilon_{\text{ff}}$ as a function gas metallicity and UV flux. Typical depletion time in star-forming cells in the simulation ($\approx 70 - 500$ Myr) is similar to that measured in the individual star-forming regions in the Milky Way (e.g., Heiderman et al. 2010; Lada et al. 2010, 2012; Evans et al. 2014). The figures show that characteristic depletion time does not depend on gas metallicity and exhibits only a weak trend with the UV flux.

We note that the width of the star-formation weighted rate distribution shown in Figures 4 and Figure 5 is comparable to the ≈ 0.3 dex scatter of ϵ_{ff} estimated by Hu et al. (2022) for observed star-forming clouds. However, previous studies indicated that the evolution of star-forming cloud properties can contribute significantly to the apparent scatter of ϵ_{ff} estimated in observations. For example, Grisdale et al. (2019) show that dramatic changes in the properties of star-forming clouds during their evolution contribute most of the scatter in ϵ_{ff} values estimated for star-forming molecular clouds the way it is done in observations. Notably, they show that the distribution of ϵ_{ff} estimated in observations by Lee et al. (2016) can be matched

¹ Free-space UV flux is the flux at a given location not attenuated by *local* extinction. Krumholz et al. (2009), for example, use free-space flux to mean the flux incident on molecular clouds. In our simulations, the radiative transfer

calculations do not include absorption by H_2 lines and thus do not model the radiation field self-consistently inside molecular-rich regions and have to rely on the subgrid model. In this case, the free-space flux is the flux returned by the radiative transfer solver and has the physical meaning of the incident field on the molecular gas.

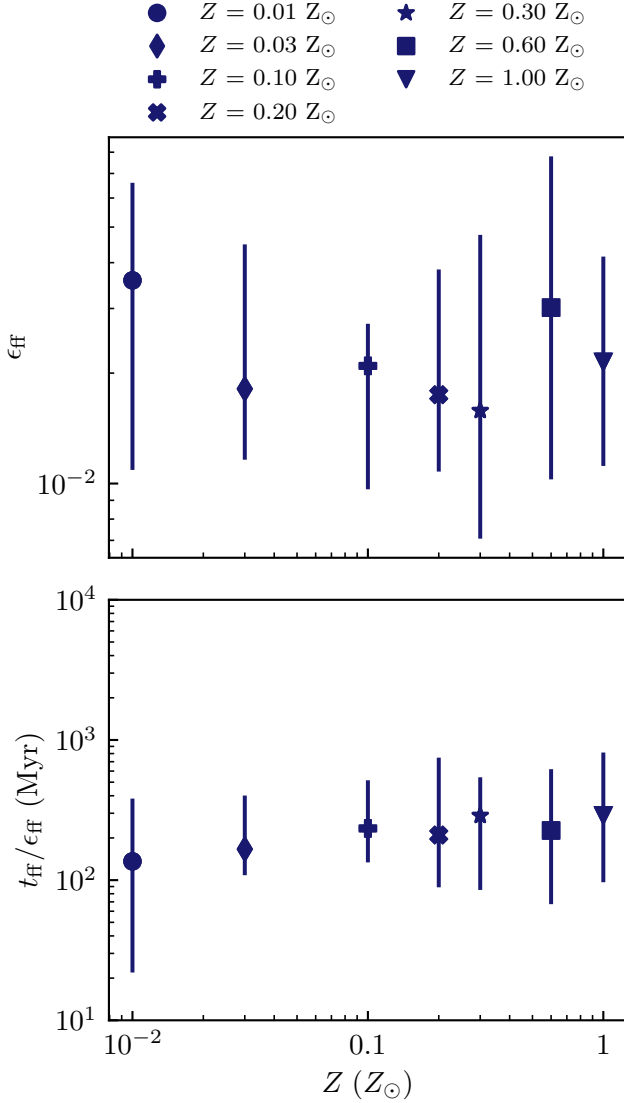


FIG. 4.— The star formation rate-weighted mean ϵ_{ff} (top) and depletion time (bottom) as a function of gas metallicity in the simulation grid cells (i.e. ~ 10 pc scale). Error bars correspond to the 16th and 84th percentiles of the distribution.

in a simulation in which intrinsic ϵ_{ff} in star-forming molecular gas is fixed to a constant value.

3.2. Star formation efficiency as a function of local environment properties on 500 pc scale

We examine the star formation efficiency per free-fall time (ϵ_{ff}), the free-fall time (t_{ff}), and the depletion time ($t_{\text{ff}}/\epsilon_{\text{ff}}$), averaged in patches of 500 pc size, as a function of metallicity, UV flux, and baryon (stars and gas) surface density. Namely, we compute the weighted medians² of these quantities using the normalized local star formation rate in each cell as a weight. We also only use the cells with $\alpha_{\text{vir}} \leq 15$, which contribute the bulk of the total star formation in each simulated galaxy. Note that we actually compute the SFR-weighted averages of $1/t_{\text{ff}}$ and $\epsilon_{\text{ff}}/t_{\text{ff}}$ because the star formation rate is proportional

² We define weighted quantiles by the value corresponding to the percentile of the cumulative distribution of weights ordered by the product of the values and the weights.

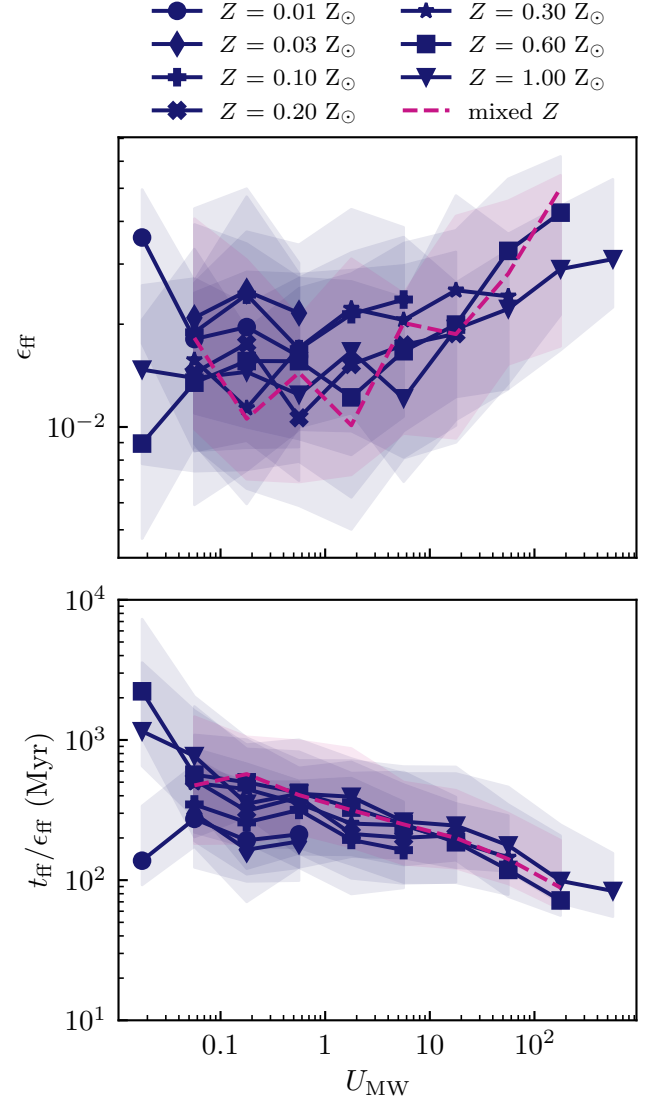


FIG. 5.— The same as Figure 4 for the dependence of each run of the simulation on the ionizing radiation field. Shaded regions correspond to the 16th and 84th percentiles of the distribution.

to these quantities. However, we plot their inverses t_{ff} and $t_{\text{ff}}/\epsilon_{\text{ff}}$ since the free-fall time and the depletion time values are more easily interpretable.

The left column of Figure 6 shows the SFR-weighted median ϵ_{ff} , t_{ff} , and $t_{\text{ff}}/\epsilon_{\text{ff}}$ for all star-forming grid cells in 500 pc patches in the runs of different metallicity. Similar to the ϵ_{ff} on ~ 10 pc scale, the figure shows that the median efficiency per free-fall time on 500 pc scale does not exhibit any trend with gas metallicity and ranges in $\epsilon_{\text{ff}} \approx 0.007 - 0.04$ – the values broadly consistent with efficiencies inferred from observations on similar scales (e.g., McKee & Ostriker 2007; Schinnerer & Leroy 2024, and references therein). The free-fall time and depletion time $t_{\text{ff}}/\epsilon_{\text{ff}}$ also do not exhibit strong trends with metallicity.

The middle column of Figure 6 shows the dependence of ϵ_{ff} , t_{ff} , and $t_{\text{ff}}/\epsilon_{\text{ff}}$ on the UV flux. The median ϵ_{ff} exhibits a trend with U_{MW} , but the trend is very weak with ϵ_{ff} increasing by a factor of \sim three as UV flux increases by three orders of magnitude. This correlation does not reflect causation, but the

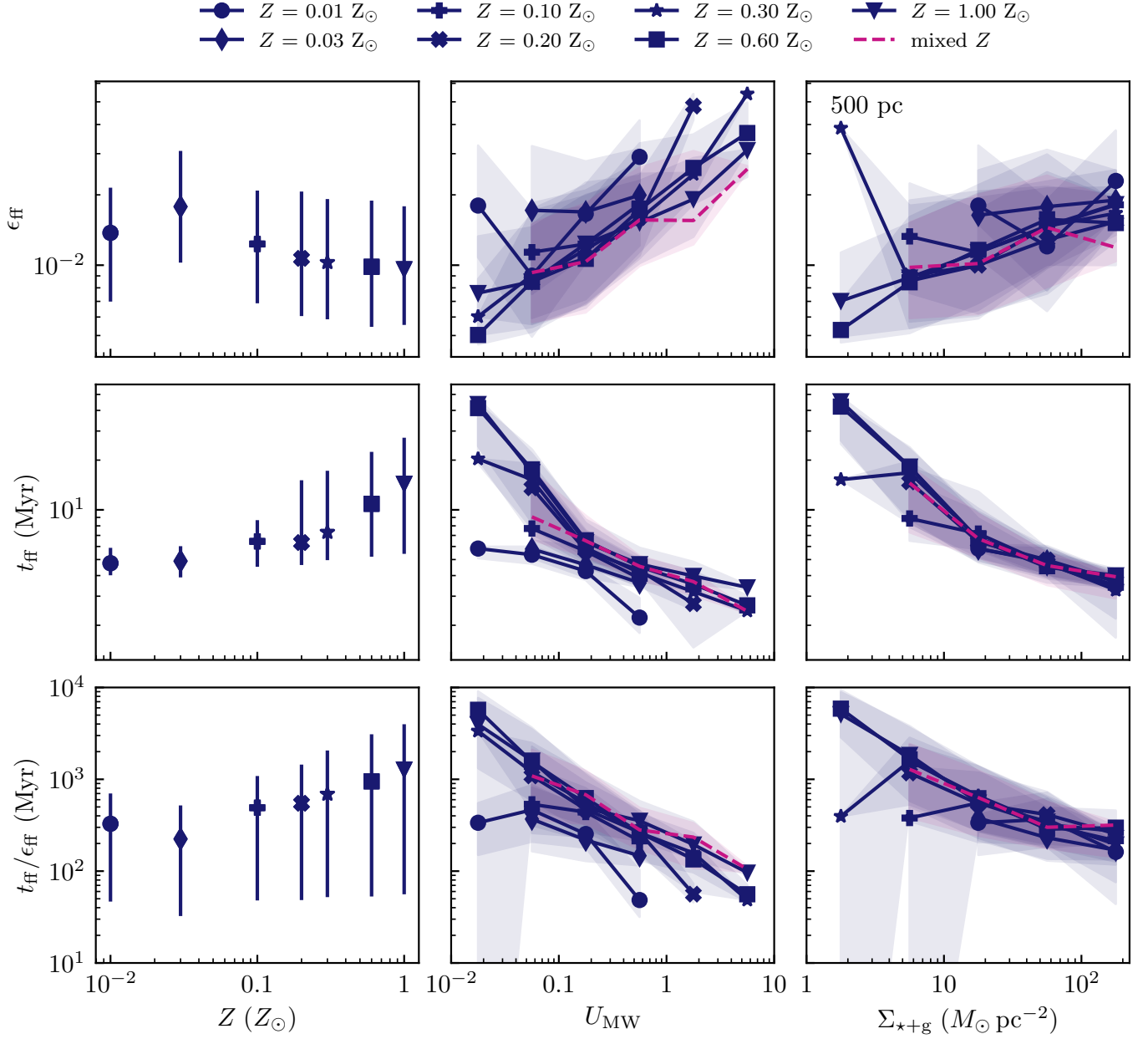


FIG. 6.— *Top*: The star formation rate-weighted median ϵ_{ff} as a function of gas metallicity (left), UV field strength (middle), and surface density of stars and gas (right) smoothed on 500 pc scales for each of our single Z simulation runs and the mixed Z run. *Middle*: The same as the top but for t_{ff} . *Bottom*: The same as the top but for $t_{\text{ff}}/\epsilon_{\text{ff}}$. The error bars and shaded regions correspond to the 16th and 84th percentiles of the distributions. It is notable that ϵ_{ff} , t_{ff} , and $t_{\text{ff}}/\epsilon_{\text{ff}}$ are not dependent on the gas phase metallicity and exhibit only weak trends with UV flux and gas surface density.

fact that regions with higher ϵ_{ff} have higher star formation rate and thus higher FUV flux.

Also, over the entire range, the median values of the efficiency are in the range $\approx 0.005 - 0.05$. Note that this range of values is a bit different than the range of ϵ_{ff} in the $\epsilon_{\text{ff}} - Z$ panel quoted above because averaging in bins of U_{MW} is over somewhat different gas elements than averaging in bins of Z .

There is also a weak anti-correlation of t_{ff} and U_{MW} , which can arise because t_{ff} decreases with increasing density, while U_{MW} increases with increasing gas density due to the increase of star formation rate with density. Finally, there is a weak trend of increasing t_{ff} and $t_{\text{ff}}/\epsilon_{\text{ff}}$ with increasing metallicity at a given U_{MW} .

The right column of panels of Figure 6 shows the SFR-weighted medians of ϵ_{ff} , t_{ff} , $t_{\text{ff}}/\epsilon_{\text{ff}}$ in the projected patches as a function of the baryon surface density of the patches. The density of gas and stars is directly integrated along the line-of-sight, while the statistics of ϵ_{ff} , t_{ff} , and $t_{\text{ff}}/\epsilon_{\text{ff}}$ are computed using grid cells with $\alpha_{\text{vir}} \leq 15$ and a refinement level with $\Delta x < 500$ pc.

The efficiency ϵ_{ff} shows only a weak trend with surface density. Our results thus indicate that in the simulations with the turbulence-based SFR model with realistic stellar feedback the natural result is the universality of characteristic ϵ_{ff} values of star-forming gas in environments with a wide range of metallicities, UV fluxes, and densities and over a wide range of

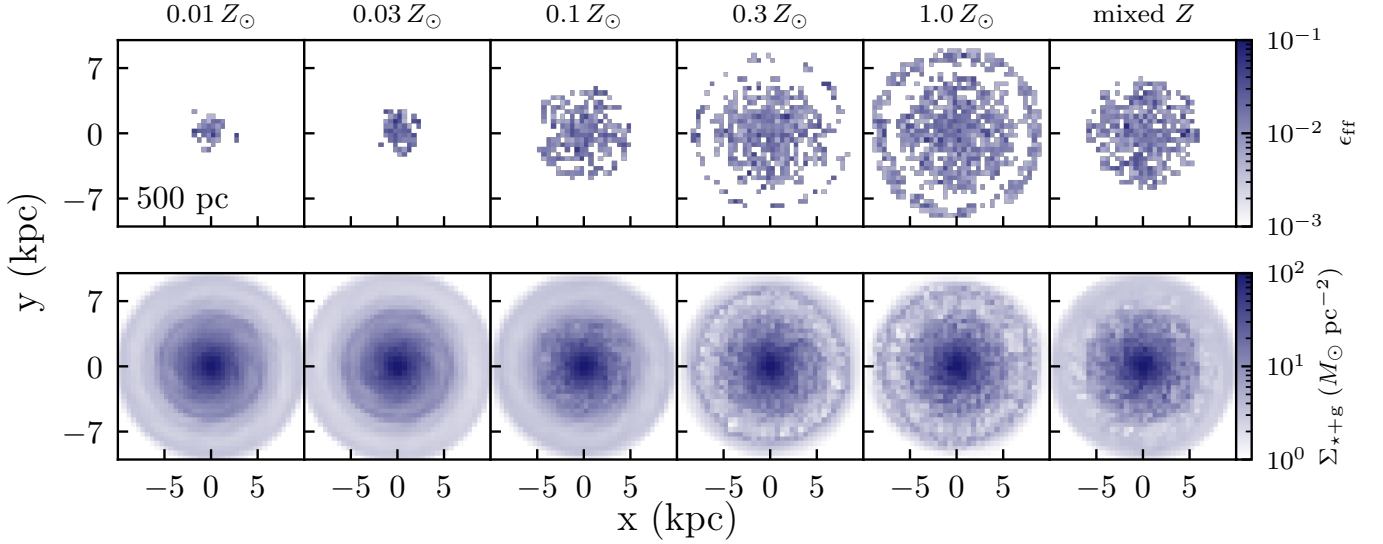


FIG. 7.— Projected face-on maps showing the mean ϵ_{ff} along the line of sight and the baryon surface density, $\Sigma_{\text{star+g}}$, on 500 pc scales for some of the runs in the simulation suite we use here.

averaging scales. This is further illustrated in Figure 7, which shows the face-on projected maps of ϵ_{ff} along with the maps of baryon surface density. The figure visually shows that while surface density varies by more than an order of magnitude in the inner regions of the disk, the values of ϵ_{ff} stay in a narrow range around $\epsilon_{\text{ff}} \approx 0.01$.

The median free-fall time of star-forming gas, on the other hand, shows tight, nearly metallicity-independent correlations with the UV flux and baryon surface density. This indicates that star-forming gas is denser in denser regions of the galaxy. This may be because gas in high surface density regions experiences a stronger gravitational pull by the disk compressing it to higher densities. The trend with UV flux may reflect the positive correlation of the UV flux and star formation rate, which, in turn, correlates with gas density. These trends of t_{ff} result in similar trends of the depletion time with U_{MW} and $\Sigma_{\text{star+g}}$.

4. DISCUSSION

As noted above, the characteristic values of ϵ_{ff} in our simulations arise naturally from the specific star-formation prescription based on the simulations of star formation in turbulent molecular clouds (see eq. 1 above; Padoan et al. 2012). The efficiency in this simulation-calibrated prescription is an exponential function of $\sqrt{\alpha_{\text{vir}}}$, where α_{vir} is the virial parameter given by eq. 2, which measures the relative importance of turbulent and thermal pressure relative to gravitational force.

The characteristic values of $\epsilon_{\text{ff}} \approx 0.01 - 0.1$ measured in the simulations thus correspond to the characteristic values of $\alpha_{\text{vir}} \approx 3 - 10$, which are set by the dynamics of the ISM gas and stellar feedback that affects the thermal and turbulent pressure of the gas.

Large-scale ISM flows lead to compression and expansion of the gas and fluctuations of α_{vir} (e.g., Semenov et al. 2017). As a local compression decreases α_{vir} locally, ϵ_{ff} grows as $\propto \exp(-\sqrt{\alpha_{\text{vir}}})$. This growth is accompanied by the growth of star formation rate and associated stellar feedback, which increases local thermal and, importantly, turbulent pressure. This limits the decrease of α_{vir} and leads to self-regulation of its values to the characteristic range of $\alpha_{\text{vir}} \approx 3 - 10$. Part

of the reason behind the narrow range of α_{vir} is the fact that during compression and expansion due to large-scale flows and feedback turbulence often evolves adiabatically, $\sigma \propto n^{1/3}$, and the virial parameter changes only mildly during such evolution, $\alpha_{\text{vir}} \propto \sigma^2/n \propto n^{-1/3}$. The characteristic values of $\epsilon_{\text{ff}} \approx 0.01 - 0.1$ in our simulations are thus the result of the star formation prescription and the stellar feedback model adopted in our simulations.

This also allows us to interpret the universality of ϵ_{ff} in environments of different metallicity, UV flux, and densities demonstrated above. The pressure and α_{vir} in star-forming regions in these simulations are dominated by turbulence. The turbulent energy is driven by gas compression by large-scale flows and the dissipation on the turbulent crossing time scale. Both processes do not depend on the metallicity, UV flux, or density. In contrast, the gas cooling and heating, and therefore thermal pressure, do depend on these properties and thus, when α_{vir} is dominated by the thermal pressure, the efficiency per free-fall time varies more strongly with the properties of the environment. This is illustrated explicitly in the Appendix A, where we show ϵ_{ff} as a function of metallicity, UV flux, and surface density in simulations, in which subgrid turbulence is not modeled and its contribution to α_{vir} is ignored. The turbulence thus plays an important role in making ϵ_{ff} value range universal.

The values of ϵ_{ff} and their universality exhibited in our simulations are consistent with the typical values of $\approx 0.01 - 0.1$ estimated for observed gas in diverse environments and averaging scales (e.g., García-Burillo et al. 2012; Utomo et al. 2018; Sun et al. 2023). Estimates of ϵ_{ff} from the star-forming sub-pc cores to giant molecular clouds on tens of pc scales are $\approx 0.01 - 0.1$ (e.g., Krumholz & Tan 2007; Evans et al. 2014; Pophrel et al. 2021; Hu et al. 2022). Similar values of ϵ_{ff} are estimated on the scales of hundreds of pc in other galaxies with a diverse range of metallicities and surface densities (e.g., Leroy et al. 2008; Utomo et al. 2018; Teng et al. 2024). Our results indicate that these characteristic values of ϵ_{ff} and their universality can be plausibly explained by the turbulence-driven and feedback-regulated properties of star-forming regions.

We note, however, that comparing detailed distribution of

ϵ_{ff} estimated in observations and simulations is not straightforward. In simulations, instantaneous values of ϵ_{ff} are considered, while in observations, these values are estimated using instantaneous gas properties and star formation rate indicators that are sensitive to star formation over a certain time scale. The gas density is expected to evolve strongly as the star formation and feedback proceed in a given region (Feldmann & Gnedin 2011). The large apparent scatter of observational estimates of ϵ_{ff} thus largely reflects diverse evolutionary stages of the regions in which these estimates are made (e.g., Feldmann & Gnedin 2011; Lee et al. 2016; Grisdale et al. 2019). Nevertheless, the simulations shed light on why the characteristic average values of ϵ_{ff} do not vary with environment properties.

Finally, we note that recently Semenov et al. (2024) and Segovia Otero et al. (2024) presented results of cosmological galaxy formation simulations of Milky Way-sized galaxies with the same prescription for ϵ_{ff} given by equations 1 and 2 above. In both studies, the authors found that the average ϵ_{ff} of the simulated galaxies was $\sim 1\%$, although rapidly changing conditions during early stages of evolution result in significant efficiency fluctuations around this characteristic value. In particular, Semenov et al. (2024) showed that fluctuations of ϵ_{ff} are the dominant source of burstiness of star formation during the early stages of galaxy evolution.

5. SUMMARY AND CONCLUSIONS

In this study, we analyze high-resolution simulations of gas dynamics and star formation in an isolated disk dwarf galaxy with an explicit model for unresolved turbulence and turbulence-based star formation prescription calibrated on MHD simulations of turbulent molecular clouds. As demonstrated by Semenov et al. (2021), the star formation and feedback model used in the simulations reproduces star formation and gas correlations in observed galaxy NGC 300 in fine detail. We use a suite of simulations at different metallicities to examine the characteristic values of the star formation efficiency per free-fall time, ϵ_{ff} , and its variations with local environment properties, such as metallicity, UV flux, and surface density. Our results and conclusions can be summarized as follows.

1. We show that the star formation efficiency per free-fall time in ≈ 10 pc star-forming regions of the simulated disks has characteristic values in the range $\epsilon_{\text{ff}} \approx 0.01 - 0.1$ (Figures 2 and 3). We show that the characteristic values of ϵ_{ff} do not vary with metallicity and exhibit only a very weak trend with UV flux (Figures 4 and 5).
2. Likewise, we show that ϵ_{ff} estimated on a 500 pc scale does not vary with metallicity and shows only weak trends with average UV flux and gas surface density estimated at this scale (Figures 6 and 7).
3. The characteristic values of $\epsilon_{\text{ff}} \approx 0.01 - 0.1$ arise naturally in the simulations as a result of the gas dynamics leading to gas compression and ensuing stellar feedback that injects thermal and turbulent energy into the gas. The compression and feedback regulate the virial parameter, α_{vir} , in star-forming regions, limiting it to the range $\alpha_{\text{vir}} \approx 3 - 10$ (see discussion in Section 4). Turbulence plays an important role in the universality of ϵ_{ff} because turbulent energy driven by gas dynamics and feedback and its dissipation are not sensitive to the standard metallicity and UV flux cooling and heating processes that affect thermal energy.

4. We show explicitly that ϵ_{ff} values do depend on the metallicity and UV flux in simulations where turbulent pressure contribution to the virial parameter is ignored (Figure 8).

The efficiency per free-fall time and its universality are similar to the values of observed star-forming regions in different environments and galaxies. This indicates that the universality of observational estimates of ϵ_{ff} can be plausibly explained by the turbulence-driven and feedback-regulated properties of star-forming regions. In the future, it will be important to forward model observational measurements using simulations taking into account evolutionary effects on the estimates of ϵ_{ff} .

The authors thank the referees for comments that improved the manuscript. A.K. was supported by the National Science Foundation grant AST-1911111 and NASA ATP grant 80NSSC20K0512. V.S. is grateful for the support provided by Harvard University through the Institute for Theory and Computation Fellowship. The simulations used in this work were carried out on the Midway cluster maintained by the University of Chicago Research Computing Center. Analyses presented in this paper were greatly aided by the following free software packages: NumPy (Harris et al. 2020), SciPy (Jones et al. 2001), Matplotlib (Hunter 2007), AstroPy (Astropy Collaboration et al. 2013, 2018, 2022) and yt (Turk et al. 2011). We have also used the Astrophysics Data Service (ADS) and arXiv preprint repository extensively during this project and the writing of the paper.

APPENDIX

A. TURBULENCE-FREE STAR FORMATION

To better understand the mechanism driving the uniformity of the star formation efficiency with varying ISM properties (metallicity, UV field strength, and surface density of gas and stars), we re-run five of the single metallicity simulations ($Z = 0.01, 0.03, 0.1, 0.3$, and $1 Z_{\odot}$) from the same initial conditions as the fiducial simulations introduced in Section 2, turning off subgrid turbulence and any tracking of turbulent energy. The non-turbulent virial parameter, $\alpha_{\text{vir,nt}}$, is then defined taking $\sigma_{\text{tot}} = c_s$, rather than $\sigma_{\text{tot}} = \sqrt{\sigma_t^2 + c_s^2}$ as in the default Padoan et al. (2012) model (see Eq. 2), effectively isolating the behavior and effects of thermal motions in star-forming gas. After the runs each proceed for ~ 100 Myr (approximately a crossing time), ϵ_{ff} is then recomputed using $\alpha_{\text{vir,nt}}$ for the non-turbulent case. We denote this non-turbulent star formation efficiency per free-fall time as $\epsilon_{\text{ff,nt}}$. Similarly, the turbulence-free star formation rate is defined as $\dot{M}_{\star} = \epsilon_{\text{ff,nt}} \dot{M}_{\text{gas}} / t_{\text{ff}}$.

All other analysis is done in the same way as in Section 3.1, and we do not change any of the physics associated with star formation or feedback within the simulation. For direct comparison between Figure 6 and 8, we make the same cut of $\alpha_{\text{vir}} \leq 15$, with cells weighted by their star formation rates.

The dependence of $\epsilon_{\text{ff,nt}}$ on gas phase metallicity is shown on the left in Figure 8. In the turbulence-free case, ϵ_{ff} dependence on metallicity is noticeably stronger than in the fiducial simulations. This is likely due to the importance of thermal motions in defining $\alpha_{\text{vir,nt}}$. Even selecting only for star-forming regions ($\alpha_{\text{vir}} \leq 15$), low metallicity gas will be warmer than higher Z gas given the less efficient cooling in low metallicity gas. In this case, the thermal motions defined by c_s will be greater in

low Z gas, increasing $\alpha_{\text{vir,nt}}$ and driving $\epsilon_{\text{ff,nt}}$ down compared with ϵ_{ff} . This leads to ϵ_{ff} varying increasing steadily with increasing gas phase metallicity.

Likewise, Figure 8 shows that in the simulations without subgrid turbulence ϵ_{ff} depends significantly on the local UV flux and gas surface density (the middle and right panels). The middle panel of Figure 8. The figure shows that $\epsilon_{\text{ff,nt}}$ increases with increasing U_{MW} and surface density of gas and stars

(averaged on 500 pc) due to the positive correlation between U_{MW} and density and star formation rate. The significant dependence of the efficiency on metallicity at specific values of U_{MW} and surface density are also apparent in these panels.

Note that stellar feedback still operates in the runs without turbulence. Thus, as gas cools and reaches higher densities star formation rate increases and so does associated stellar feedback. The feedback prevents runaway collapse and disperses star-forming regions.

REFERENCES

- Agertz, O., & Kravtsov, A. V. 2015, *ApJ*, 804, 18, doi: [10.1088/0004-637X/804/1/18](https://doi.org/10.1088/0004-637X/804/1/18)
- Astropy Collaboration, Robitaille, T. P., Tollerud, E. J., et al. 2013, *A&A*, 558, A33, doi: [10.1051/0004-6361/201322068](https://doi.org/10.1051/0004-6361/201322068)
- Astropy Collaboration, Price-Whelan, A. M., Sipőcz, B. M., et al. 2018, *AJ*, 156, 123, doi: [10.3847/1538-3881/aabc4f](https://doi.org/10.3847/1538-3881/aabc4f)
- Astropy Collaboration, Price-Whelan, A. M., Lim, P. L., et al. 2022, *apj*, 935, 167, doi: [10.3847/1538-4357/ac7c74](https://doi.org/10.3847/1538-4357/ac7c74)
- Bertoldi, F., & McKee, C. F. 1992, *ApJ*, 395, 140, doi: [10.1086/171638](https://doi.org/10.1086/171638)
- Brucy, N., Hennebelle, P., Colman, T., Klessen, R. S., & Le Yhuelic, C. 2024, *A&A*, 690, A44, doi: [10.1051/0004-6361/202450525](https://doi.org/10.1051/0004-6361/202450525)
- Draine, B. T. 1978, *ApJS*, 36, 595, doi: [10.1086/190513](https://doi.org/10.1086/190513)
- Elmegreen, B. G. 2002, *ApJ*, 577, 206, doi: [10.1086/342177](https://doi.org/10.1086/342177)
- Evans, Neal J., I., Heiderman, A., & Vutisalchavakul, N. 2014, *ApJ*, 782, 114, doi: [10.1088/0004-637X/782/2/114](https://doi.org/10.1088/0004-637X/782/2/114)
- Federrath, C. 2015, *MNRAS*, 450, 4035, doi: [10.1093/mnras/stv941](https://doi.org/10.1093/mnras/stv941)
- Federrath, C., & Klessen, R. S. 2013, *ApJ*, 763, 51, doi: [10.1088/0004-637X/763/1/51](https://doi.org/10.1088/0004-637X/763/1/51)
- Feldmann, R., & Gnedin, N. Y. 2011, *ApJ*, 727, L12, doi: [10.1088/2041-8205/727/1/L12](https://doi.org/10.1088/2041-8205/727/1/L12)
- García-Burillo, S., Usero, A., Alonso-Herrero, A., et al. 2012, *A&A*, 539, A8, doi: [10.1051/0004-6361/201117838](https://doi.org/10.1051/0004-6361/201117838)
- Girma, E., & Teyssier, R. 2024, *MNRAS*, 527, 6779, doi: [10.1093/mnras/stad3640](https://doi.org/10.1093/mnras/stad3640)
- Gnedin, N. Y. 2014, *ApJ*, 793, 29, doi: [10.1088/0004-637X/793/1/29](https://doi.org/10.1088/0004-637X/793/1/29)
- Gnedin, N. Y., & Kravtsov, A. V. 2011, *ApJ*, 728, 88, doi: [10.1088/0004-637X/728/2/88](https://doi.org/10.1088/0004-637X/728/2/88)
- Grisdale, K., Agertz, O., Renaud, F., et al. 2019, *MNRAS*, 486, 5482, doi: [10.1093/mnras/stz1201](https://doi.org/10.1093/mnras/stz1201)
- Harris, C. R., Millman, K. J., van der Walt, S. J., et al. 2020, *Nature*, 585, 357, doi: [10.1038/s41586-020-2649-2](https://doi.org/10.1038/s41586-020-2649-2)
- Heiderman, A., Evans, Neal J., I., Allen, L. E., Huard, T., & Heyer, M. 2010, *ApJ*, 723, 1019, doi: [10.1088/0004-637X/723/2/1019](https://doi.org/10.1088/0004-637X/723/2/1019)
- Hu, Z., Krumholz, M. R., Pokhrel, R., & Gutermuth, R. A. 2022, *MNRAS*, 511, 1431, doi: [10.1093/mnras/stac174](https://doi.org/10.1093/mnras/stac174)
- Hunter, J. D. 2007, *Computing in Science & Engineering*, 9, 90, doi: [10.1109/MCSE.2007.55](https://doi.org/10.1109/MCSE.2007.55)
- Jones, E., Oliphant, T., Peterson, P., et al. 2001, *SciPy: Open source scientific tools for Python*. <http://www.scipy.org/>
- Kravtsov, A. V. 1999, PhD thesis, New Mexico State University
- Kravtsov, A. V., Klypin, A., & Hoffman, Y. 2002, *ApJ*, 571, 563, doi: [10.1086/340046](https://doi.org/10.1086/340046)
- Kruijssen, J. M. D., Schrubba, A., Chevance, M., et al. 2019, *Nature*, 569, 519, doi: [10.1038/s41586-019-1194-3](https://doi.org/10.1038/s41586-019-1194-3)
- Krumholz, M. R. 2014, *Phys. Rep.*, 539, 49, doi: [10.1016/j.physrep.2014.02.001](https://doi.org/10.1016/j.physrep.2014.02.001)
- Krumholz, M. R., Dekel, A., & McKee, C. F. 2012, *ApJ*, 745, 69, doi: [10.1088/0004-637X/745/1/69](https://doi.org/10.1088/0004-637X/745/1/69)
- Krumholz, M. R., & Federrath, C. 2019, *Frontiers in Astronomy and Space Sciences*, 6, 7, doi: [10.3389/fspas.2019.00007](https://doi.org/10.3389/fspas.2019.00007)
- Krumholz, M. R., & McKee, C. F. 2005, *ApJ*, 630, 250, doi: [10.1086/431734](https://doi.org/10.1086/431734)
- Krumholz, M. R., McKee, C. F., & Bland-Hawthorn, J. 2019, *ARA&A*, 57, 227, doi: [10.1146/annurev-astro-091918-104430](https://doi.org/10.1146/annurev-astro-091918-104430)
- Krumholz, M. R., McKee, C. F., & Tumlinson, J. 2009, *ApJ*, 693, 216, doi: [10.1088/0004-637X/693/1/216](https://doi.org/10.1088/0004-637X/693/1/216)
- Krumholz, M. R., & Tan, J. C. 2007, *ApJ*, 654, 304, doi: [10.1086/509101](https://doi.org/10.1086/509101)
- Lada, C. J., Forbrich, J., Lombardi, M., & Alves, J. F. 2012, *ApJ*, 745, 190, doi: [10.1088/0004-637X/745/2/190](https://doi.org/10.1088/0004-637X/745/2/190)
- Lada, C. J., Lombardi, M., & Alves, J. F. 2010, *ApJ*, 724, 687, doi: [10.1088/0004-637X/724/1/687](https://doi.org/10.1088/0004-637X/724/1/687)
- Lee, E. J., Miville-Deschênes, M.-A., & Murray, N. W. 2016, *ApJ*, 833, 229, doi: [10.3847/1538-4357/833/2/229](https://doi.org/10.3847/1538-4357/833/2/229)
- Leroy, A. K., Walter, F., Brinks, E., et al. 2008, *AJ*, 136, 2782, doi: [10.1088/0004-6256/136/6/2782](https://doi.org/10.1088/0004-6256/136/6/2782)
- Mathis, J. S., Mezger, P. G., & Panagia, N. 1983, *A&A*, 128, 212
- Mattern, M., André, P., Zavagno, A., et al. 2024, *arXiv e-prints*, arXiv:2405.15713, doi: [10.48550/arXiv.2405.15713](https://doi.org/10.48550/arXiv.2405.15713)
- McKee, C. F., & Ostriker, E. C. 2007, *ARA&A*, 45, 565, doi: [10.1146/annurev.astro.45.051806.110602](https://doi.org/10.1146/annurev.astro.45.051806.110602)
- Mouschovias, T. C. 1976a, *ApJ*, 206, 753, doi: [10.1086/154436](https://doi.org/10.1086/154436)
- . 1976b, *ApJ*, 207, 141, doi: [10.1086/154478](https://doi.org/10.1086/154478)
- Padoan, P., Haugbølle, T., & Nordlund, Å. 2012, *ApJ*, 759, L27, doi: [10.1088/2041-8205/759/2/L27](https://doi.org/10.1088/2041-8205/759/2/L27)
- Pokhrel, R., Gutermuth, R. A., Krumholz, M. R., et al. 2021, *ApJ*, 912, L19, doi: [10.3847/2041-8213/abf564](https://doi.org/10.3847/2041-8213/abf564)
- Polzin, A., Kravtsov, A. V., Semenov, V. A., & Gnedin, N. Y. 2024, *ApJ*, 966, 172, doi: [10.3847/1538-4357/ad32cb](https://doi.org/10.3847/1538-4357/ad32cb)
- Price, D. J., & Bate, M. R. 2009, *MNRAS*, 398, 33, doi: [10.1111/j.1365-2966.2009.14969.x](https://doi.org/10.1111/j.1365-2966.2009.14969.x)
- Rudd, D. H., Zentner, A. R., & Kravtsov, A. V. 2008, *ApJ*, 672, 19, doi: [10.1086/523836](https://doi.org/10.1086/523836)
- Schinnerer, E., & Leroy, A. K. 2024, *arXiv e-prints*, arXiv:2403.19843, doi: [10.48550/arXiv.2403.19843](https://doi.org/10.48550/arXiv.2403.19843)
- Segovia Otero, Á., Agertz, O., Renaud, F., et al. 2024, *arXiv e-prints*, arXiv:2410.08266, doi: [10.48550/arXiv.2410.08266](https://doi.org/10.48550/arXiv.2410.08266)
- Semenov, V. A., Conroy, C., & Hernquist, L. 2024, *arXiv e-prints*, arXiv:2410.09205, doi: [10.48550/arXiv.2410.09205](https://doi.org/10.48550/arXiv.2410.09205)
- Semenov, V. A., Kravtsov, A. V., & Gnedin, N. Y. 2016, *ApJ*, 826, 200, doi: [10.3847/0004-637X/826/2/200](https://doi.org/10.3847/0004-637X/826/2/200)
- . 2017, *ApJ*, 845, 133, doi: [10.3847/1538-4357/aa8096](https://doi.org/10.3847/1538-4357/aa8096)
- . 2018, *ApJ*, 861, 4, doi: [10.3847/1538-4357/aac6eb](https://doi.org/10.3847/1538-4357/aac6eb)
- . 2021, *ApJ*, 918, 13, doi: [10.3847/1538-4357/ac0a77](https://doi.org/10.3847/1538-4357/ac0a77)
- Sun, J., Leroy, A. K., Ostriker, E. C., et al. 2023, *ApJ*, 945, L19, doi: [10.3847/2041-8213/acbd9c](https://doi.org/10.3847/2041-8213/acbd9c)
- Teng, Y.-H., Chiang, I.-D., Sandstrom, K. M., et al. 2024, *ApJ*, 961, 42, doi: [10.3847/1538-4357/ad10ae](https://doi.org/10.3847/1538-4357/ad10ae)
- Turk, M. J., Smith, B. D., Oishi, J. S., et al. 2011, *ApJS*, 192, 9, doi: [10.1088/0067-0049/192/1/9](https://doi.org/10.1088/0067-0049/192/1/9)
- Utomo, D., Sun, J., Leroy, A. K., et al. 2018, *ApJ*, 861, L18, doi: [10.3847/2041-8213/aacf8f](https://doi.org/10.3847/2041-8213/aacf8f)
- Zuckerman, B., & Evans, N. J., I. 1974, *ApJ*, 192, L149, doi: [10.1086/181613](https://doi.org/10.1086/181613)

This paper was built using the Open Journal of Astrophysics \LaTeX template. The OJA is a journal which provides fast and easy peer review for new papers in the astro-ph section of the

arXiv, making the reviewing process simpler for authors and referees alike. Learn more at <http://astro.theoj.org>.

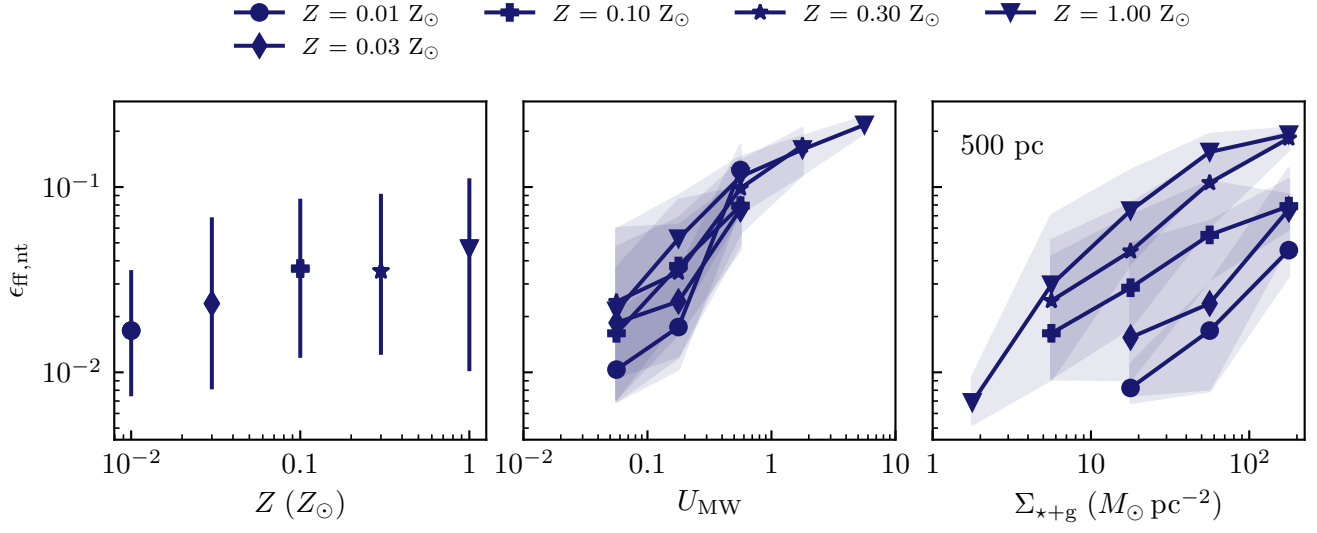


FIG. 8.— The same as the top row of Figure 6, but with turbulence turned off. The now-strong dependence of the star formation efficiency on metallicity and baryon surface density is apparent. (Note that the range of ϵ_{ff} shown here is larger than in Figure 6.)